New ultrasensitive resonant photonic platform for label-free biosensing

Francesco Dell'Olio, Donato Conteduca, Caterina Ciminelli,* and Mario Nicola Armenise

Optoelectronic Laboratory, Politecnico di Bari, Via Orabona 4. 70125, Bari, Italy
**caterina.ciminelli@poliba.it*

Abstract: A multi-analyte biosensing platform with ultra-high resolution (= 0.2 ng/mL),-which is appropriate for the detection in the human serum of a wide range of biomarkers, e.g. those allowing the lung cancer early diagnosis, has been designed. The platform is based on a new configuration of planar ring resonator. The very strong light-matter interaction enabled by the micro-cavity allows a record limit-of-detection of 0.06 pg/mm^2, five times better than the state-of-the-art. The device with footprint = 2,200 μm^2 for each ring, due to its features, has the potential to be integrated in lab-on-chip microsystems for large-scale screenings of people with high risk of developing cancer.

OCIS codes: (130.3120) Integrated optics devices; (130.6010) Sensors; (230.5750) Resonators.

References and links

1. J. A. Roth, W. K. Hong, and R. U. Komaki, eds., *Lung Cancer* (Wiley, 2014).
2. Cancer Research UK, "Lung cancer survival statistics," *http://www.cancerresearchuk.org/cancer-info/cancerstats/types/lung/survival/lung-cancer-survival-statistics#source5*
3. D. Barh, A. Carpi, M. Verma, and M. Gunduz, eds., *Cancer Biomarkers: Minimal and Noninvasive Early Diagnosis and Prognosis* (CRC Press, 2014).
4. J. Wu, Z. Fu, F. Yan, and H. Ju, "Biomedical and clinical applications of Immunoassays and immunosensors for tumor markers," TrAC-Trend Anal. Chem. **26**, 679–688 (2007).
5. S. K. Arya and S. Bhansali, "Lung cancer and its early detection using biomarker-based biosensors," Chem. Rev. **111**(11), 6783–6809 (2011).
6. M.-C. Estevez, M. Alvarez, and L. M. Lechuga, "Integrated optical devices for lab-on-a-chip biosensing applications," Laser Photonics Rev. **6**(4), 463–487 (2012).
7. P. V. Lambeck, "Integrated optical sensors for the chemical domain," Meas. Sci. Technol. **17**(8), R93–R116 (2006).
8. K. Schmitt, B. Schirmer, C. Hoffmann, A. Brandenburg, and P. Meyrueis, "Interferometric biosensor based on planar optical waveguide sensor chips for label-free detection of surface bound bioreactions," Biosens. Bioelectron. **22**(11), 2591–2597 (2007).
9. C. Ciminelli, C. M. Campanella, F. Dell'Olio, C. E. Campanella, and M. N. Armenise, "Label-free optical resonant sensors for biochemical applications," Prog. Quantum Electron. **37**(2), 51–107 (2013).
10. D.-X. Xu, M. Vachon, A. Densmore, R. Ma, A. Delâge, S. Janz, J. Lapointe, Y. Li, G. Lopinski, D. Zhang, Q. Y. Liu, P. Cheben, and J. H. Schmid, "Label-free biosensor array based on silicon-on-insulator ring resonators addressed using a WDM approach," Opt. Lett. **35**(16), 2771–2773 (2010).
11. H. J. Lee, Y. T. Kim, P. J. Park, Y. S. Shin, K. N. Kang, Y. Kim, and C. W. Kim, "A novel detection method of non-small cell lung cancer using multiplexed bead-based serum biomarker profiling," J. Thorac. Cardiovasc. Surg. **143**(2), 421–427 (2012).
12. C. E. Hirales Casillas, J. M. Flores Fernández, E. P. Camberos, E. J. Herrera López, G. L. Pacheco, and M. M. Velázquez, "Current status of circulating protein biomarkers to aid the early detection of lung cancer," Future Oncol. **10**(8), 1501–1513 (2014).
13. K. De Vos, I. Bartolozzi, E. Schacht, P. Bienstman, and R. Baets, "Silicon-on-Insulator microring resonator for sensitive and label-free biosensing," Opt. Express **15**(12), 7610–7615 (2007).
14. K. F. Palmer and D. Williams, "Optical properties of water in the near infrared," J. Opt. Soc. Am. **64**(8), 1107–1110 (1974).
15. A. Gondarenko, J. S. Levy, and M. Lipson, "High confinement micron-scale silicon nitride high Q ring resonator," Opt. Express **17**(14), 11366–11370 (2009).
16. O. Parriaux and G. J. Veldhuis, "Normalized analysis for the sensitivity optimization of integrated optical evanescent-wave sensors," J. Lightwave Technol. **16**(4), 573–582 (1998).
17. F. Dell'Olio and V. M. N. Passaro, "Optical sensing by optimized silicon slot waveguides," Opt. Express **15**(8), 4977–4993 (2007).

#242374 Received 4 Jun 2015; revised 25 Sep 2015; accepted 25 Sep 2015; published 23 Oct 2015

18. Y. H. Tan, M. Liu, B. Nolting, J. G. Go, J. Gervay-Hague, and G. Y. Liu, "A nanoengineering approach for investigation and regulation of protein immobilization," ACS Nano **2**(11), 2374–2384 (2008).
19. M. G. Scullion, A. Di Falco, and T. F. Krauss, "Slotted photonic crystal cavities with integrated microfluidics for biosensing applications," Biosens. Bioelectron. **27**(1), 101–105 (2011).
20. C. Rivet, H. Lee, A. Hirsch, S. Hamilton, and H. Lu, "Microfluidics for medical diagnostics and biosensors," Chem. Eng. Sci. **66**(7), 1490–1507 (2011).
21. K. F. Smith, R. A. Harrison, and S. J. Perkins, "Structural comparisons of the native and reactive-centre-cleaved forms of α_1-antitrypsin by neutron- and X-ray-scattering in solution," Biochem. J. **267**(1), 203–212 (1990).
22. K. Dohmoto, S. Hojo, J. Fujita, Y. Yang, Y. Ueda, S. Bandoh, Y. Yamaji, Y. Ohtsuki, N. Dobashi, T. Ishida, and J. Takahara, "The role of caspase 3 in producing cytokeratin 19 fragment (CYFRA21-1) in human lung cancer cell lines," Int. J. Cancer **91**(4), 468–473 (2001).
23. Z. Laron, "Insulin-like growth factor 1 (IGF-1): a growth hormone," J. Clin. Pathol.: Mol. Pathol. **54**(5), 311–316 (2001).
24. R. Alam, S. Stafford, P. Forsythe, R. Harrison, D. Faubion, M. A. Lett-Brown, and J. A. Grant, "RANTES is a chemotactic and activating factor for human eosinophils," J. Immunol. **150**(8 Pt 1), 3442–3448 (1993).
25. A. J. Luft and F. L. Lorscheider, "Structural analysis of human and bovine alpha-fetoprotein by electron microscopy, image processing, and circular dichroism," Biochemistry **22**(25), 5978–5981 (1983).
26. Y. Kurihara, M. Takama, T. Sekiya, Y. Yoshihara, T. Ooya, and T. Takeuchi, "Fabrication of carboxylated silicon nitride sensor chips for detection of antigen-antibody reaction using microfluidic reflectometric interference spectroscopy," Langmuir **28**(38), 13609–13615 (2012).
27. A. Yariv, "Universal relations for coupling of optical power between microresonators and dielectric waveguides," Electron. Lett. **36**(4), 321–322 (2000).
28. K. Gazzaz and P. Berini, "Theoretical biosensing performance of surface plasmon polariton Bragg gratings," Appl. Opt. **54**(7), 1673–1690 (2015).
29. M. J. Liu, *Photonic devices* (Cambridge University, 2005).
30. R. C. Alferness and P. S. Cross, "Filter characteristics of codirectionally coupled waveguides with weighted coupling," IEEE J. Quantum Electron. **14**(11), 843–847 (1978).
31. K. B. Gylfason, C. F. Carlborg, A. Kaźmierczak, F. Dortu, H. Sohlström, L. Vivien, C. A. Barrios, W. van der Wijngaart, and G. Stemme, "On-chip temperature compensation in an integrated slot-waveguide ring resonator refractive index sensor array," Opt. Express **18**(4), 3226–3237 (2010).

1. Introduction

Protein biomarkes are very powerful tools in early diagnosis and monitoring of very serious pathologies, e.g., cancer, cardiovascular diseases, and neurological disorders. In oncology, the interest towards the use of biomarkes is quickly growing, with a strong research effort focused on the most common types of cancers, whose early detection dramatically increases the survival rate. For example, it is well recognized that early diagnosis of lung cancer [1], which is the leading cause of cancer death, is crucial in increasing the survival rate of patients. In UK, the one-year survival from lung cancer is 71% if the pathology is diagnosed at stage I, when the tumor is small and not spread to any lymph node, while it decreases down to 17% if the diagnosis is achieved at the stage IV, when the cancer has spread to more than one part of the lung or other distant parts of the body [2].

The availability of easy-to-use, reliable, and low-cost lab-on-chip microsystems for cancer biomarkers detection in easy collectable biologic fluids, e.g. blood, urine, and saliva, could significantly improve the percentage of early-detected cancers [3], especially if those microsystems are capable of simultaneously detecting several biomarkers. In fact, the detection of a single cancer marker at abnormal concentration usually has poor diagnostic value while the identification of abnormalities relevant to the concentration of some properly selected biomarkers is strongly correlated to the actual existence of the neoplastic disease [4]. In addition, such lab-on-chip microsystems could allow the diagnosis of sub-millimeter tumors that are not visible by the conventional imaging techniques, e.g. computerized axial tomography, magnetic resonance imaging, and positron emission tomography [5].

The features of label-free integrated optical biosensors [6], in terms of multi-analyte detection, sensitivity, selectivity, immunity to external disturbances, response time, and footprint make them very attractive key building blocks of the above mentioned microsystems.

The operating principle of label-free integrated optical biosensors is based on the chemical binding between the unlabeled target molecule, the lung cancer biomarkers in the designed device, and the functionalization adlayer on the sidewalls of the device waveguide. The binding modifies the physical properties of the adlayer, mainly its thickness, and thus the

#242374 Received 4 Jun 2015; revised 25 Sep 2015; accepted 25 Sep 2015; published 23 Oct 2015

effective index of the optical mode propagating within the waveguide. This change in the effective index can be accurately read out by either resonant or interferometic techniques. In fact, the most common configurations of label-free integrated optical biosensors are based on interferometers, especially Mach-Zehnder and Young interferometers [7,8], or resonant cavities [9], such as ring resonators and photonic crystal micro-cavities. Although some interferometric biosensors exhibit a very good limit-of-detection (LOD), about 0.01 pg/mm^2, their too large footprint (> 1,000 mm^2) makes them unsuitable for multi-analyte detection. The resonant configurations have a footprint < 0.1 mm^2 and their use in the context of multi-analyte detection is well established. Among the chip-scale integrated optical resonant biosensors, the best LOD (= 0.3 pg/mm^2) has been demonstrated by a ring resonator with a footprint less than 0.002 mm^2, whose waveguide is a silicon wire having a width of 450 nm and height of 260 nm [10]. The optical mode propagating within the micro-cavity is the fundamental quasi-TM one and the sensor resolution, i.e. the minimal detectable concentration of the analyte, is 20 pM = 1 ng/mL

In this paper, we report on the design of a new resonant label-free integrated optical biosensor for protein biomarker detection, whose key building block is a ring resonator with a novel configuration enabling a very strong interaction between the propagating mode and the molecular adlayer where the recognition of the target molecule take place. The ring is evanescently coupled to a straight bus waveguide so that the multi-analyte detection can be easily implemented coupling several rings with different radii to the same bus [10], as shown in Fig. 1.

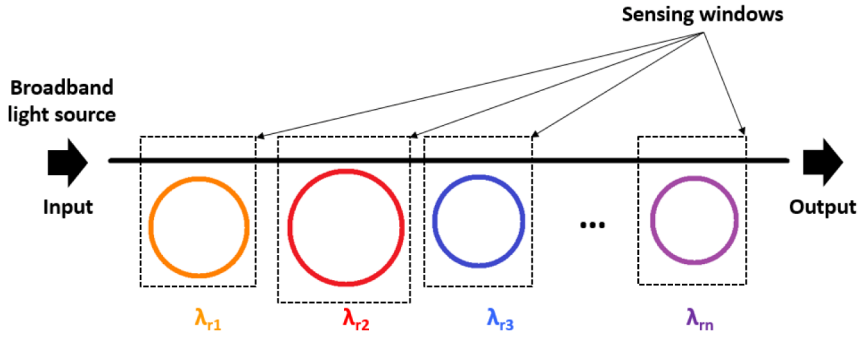

Fig. 1. Configuration of the multi-analyte biosensor.

At the input of the straight bus waveguide a broadband light beam is launched. The spectrum of the beam coming out form the bus exhibits several minima corresponding to the resonance frequencies λ_{r1}, λ_{r2},…, λ_{rn} of the n rings. The shift in the resonance frequencies of the rings, due to the binding between the target molecules and the functionalization layers (chemically different for each ring), is measured by processing the optical spectrum at the bus output. Alternatively, the device can be excited by a fast-tunable laser and a low-noise photodiode at the output can be used to evaluate the resonance spectrum of the rings. Each ring is included in a sensing window filled by the biologic fluid, which is typically an aqueous solution.

The sensor operating wavelength has been selected aiming at identifying a tradeoff between the minimization of the absorption loss due to the aqueous solution and the availability of high-performance broadband light sources at the operating wavelength. Due to the latter requirement, two possible operating wavelengths have been compared, 1300 nm and 1550 nm. Since the water optical absorption is larger at 1550 nm than 1300 nm, we have assumed the operating wavelength as equal to 1300 nm.

The sensor design is focused on a specific application, i.e. the lung cancer early diagnosis through the concentration measurement of properly selected biomarkers in the human serum. The basic concept of the device can be easily applied to the development of label-free biosensors for the high-resolution sensing of a wide range of protein biomarkers.

#242374 Received 4 Jun 2015; revised 25 Sep 2015; accepted 25 Sep 2015; published 23 Oct 2015

In [11] a set of five serum proteins capable of predicting the lung cancer with very good accuracy has been identified. The test implies the detection of Alpha-1 antitrypsin (A1AT), cytokeratin fragment 21-1 (Cyfra 21–1), insulin-like growth factor 1 (IGF1), regulated upon activation normal T cell expressed and secreted (RANTES), and alpha-fetoprotein (AFP) in the human serum with resolution 0.2 ng/mL. Alternative biomarker panels for lung cancer early detection are listed in [12].

We have designed the biosensor so that it is able to perform the above mentioned detection test. Thus it include five rings, each sensitive to one of the protein biomarkers. The rings, having different radius, have been properly designed to match the requirement in terms of resolution. The concept developed in this paper can be easily applied for the detection with ultra-high resolution of other sets of target molecules for cancer early detection or alternative purposes.

2. Design of the waveguide

The cross section of the waveguide forming the rings and the bus is shown in Fig. 2. It is a conventional silicon nitride strip waveguide on a silicon oxide substrate including a hollow region with a reversed T shape, which is properly designed to enhance the light-matter interaction. That hollow region, which is filled by the aqueous solution, consist of a horizontal slot and a vertical one. All the boundaries of the Si_3N_4 waveguide that are exposed to the aqueous solution are functionalized by a proper adlayer. We denote with w_T and h_T the total width and height of the waveguide, respectively. The width and height of the horizontal slot are w_S and h_S, respectively. The width of the vertical slot allowing filling the horizontal one is denoted as w_V. We assume that the refractive index of SiO_2 and Si_3N_4 at the operating wavelength are 1.45 and 1.98, respectively. As in [13], we assume that the refractive index of the functionalization layer n_{FL} is 1.45. For the solution, we assume the complex refractive index of water at the operating wavelength, i.e. $1.324 + (1.38\text{x}10^{-5}\text{i})$ [14]. The electromagnetic study of the waveguide, with the accurate calculation of the propagating modes effective index n_{eff}, has been carried out by the finite element method (FEM).

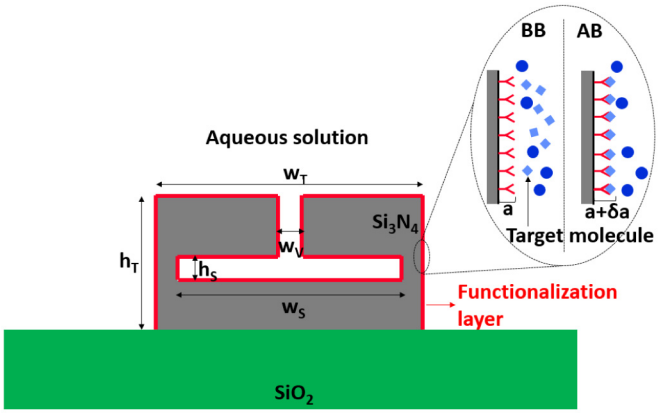

Fig. 2. Waveguide configuration. The inset shows the functionalization adlayer and the different molecules in the aqueous solution before the binding (BF) and after the binding (AB). The selective binding between the target molecules and the functionalization layer is shown. The average thickness of the adlayer is a before the binding and $(a + \delta a)$ after the binding.

For $w_T \leq 1000$ nm and $h_T \leq 500$ nm, the guiding structure supports just one quasi-TM mode. The fundamental quasi-TM mode is fully confined in the hollow region and its maximum is very close to the functionalization layer.

Experimental results [15] show that the scattering loss in a Si_3N_4 ring resonator can be less than 0.1 dB/cm by properly optimizing the fabrication process. Our FEM simulations allow to conclude that the absorption loss of the waveguide, due to the water optical absorption, is about 1.4 dB/cm and the waveguide bending loss is negligible if the bending radius is ≥ 20

#242374 Received 4 Jun 2015; revised 25 Sep 2015; accepted 25 Sep 2015; published 23 Oct 2015

μm. Thus, assuming a bending radius ≥ 20 μm, the propagation loss of the waveguide can be assumed as equal to 1.4 dB/cm.

In label-free integrated optical biosensors, the analyte detection is due to the binding between the molecules forming the functionalization adlayer and the target molecules in the solution. When the target molecules are detected, the average thickness *a* of the functionalization layer increases. Thus to enhance the LOD of those biosensors, the waveguide surface sensitivity, defined as $\partial n_{eff}/\partial a$ [16] should be maximized. At the state-of-the-art, the most sensitive waveguides are the silicon photonic wires and the silicon slot guiding structures. The surface sensitivity of those waveguides is less than 0.0005 nm^{-1} [17].

Focusing our attention on the fundamental quasi-TM mode, which is the most sensitive mode to the change in the adlayer thickness because it is well confined in the horizontal slot, we have optimized the waveguide in Fig. 2 by maximizing its surface sensitivity. We observed that the sensitivity increases as w_S increases, but too large values of w_S with respect to w_T can compromise the mechanical stability of the device. Thus, we have kept constant w_S at $0.8w_T$. The maximization of the surface sensitivity demands the minimization of w_V but too narrow values of this geometrical parameter prevent the possibility of manufacturing the waveguide. Then we have assumed $w_V = 0.1w_T$. The total height h_T has been varied in the range 300 nm – 500 nm (step = 25 nm), w_T has been varied in the range 800 nm – 1000 nm (step = 25 nm), and h_S has been varied in the range 30 nm – 80 nm (step = 5 nm). Those variation ranges assures that only one quasi-TM mode is supported by the waveguide. Values of $h_S < 30$ nm have not been considered because the thickness of the functionalization layer is about 8 nm (see the details on this layers in the following of this section). The waveguide surface sensitivity has been calculated for 640 combinations of the geometrical parameters h_T, w_T, and h_S. For each combination of h_T, w_T, and h_S the surface sensitivity has been evaluated by varying *a* from 8 nm to 12 nm (step = 1 nm) and calculating the effective index of the quasi-TM for all the *a* values. By using those data the $\partial n_{eff}/\partial a$ has been easily calculated by a linear fit algorithm. Figure 3 shows some selected results of the waveguide optimization.

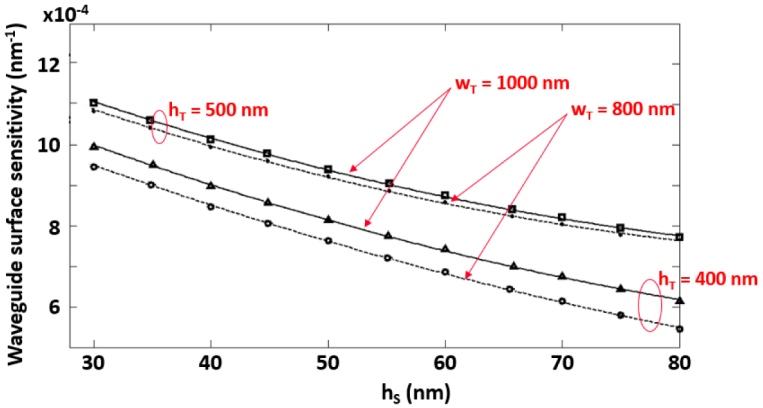

Fig. 3. Waveguide surface sensitivity vs. h_S, for h_T = 400 nm and 500 nm, w_T = 800 nm and 1000 nm.

The surface sensitivity decreases as h_S increases, while it is quite independent of w_T, mainly for large values of h_T. The waveguide total height h_T should be increased to enhance the waveguide performance. The optimum value of the sensitivity is 0.0011 nm^{-1} (more than two times better than photonic wires and slot waveguides). It is achieved for h_T = 500 nm, w_T = 1000 nm, and h_S = 30 nm. For those values of the geometrical parameters, the waveguide supports the fundamental quasi-TM mode (see Fig. 4), the fundamental quasi-TE mode, and the first-order quasi-TE mode. Thus, if a TM beam is launched in the waveguide, only the quasi-TM mode is supported by it because no polarization conversion has been observed in our 3D simulations. The effective index of the fundamental quasi-TM mode is 1.591 +

#242374 Received 4 Jun 2015; revised 25 Sep 2015; accepted 25 Sep 2015; published 23 Oct 2015

i($3.3x10^{-6}$). Since the electromagnetic field of the fundamental quasi-TM mode is well confined in the horizontal slot, we have verified that the expected incomplete functionalization of the vertical sidewalls of the waveguide has a negligible impact on the surface sensitivity, i.e. $\partial n_{eff}/\partial a$, and thus on the sensor performance.

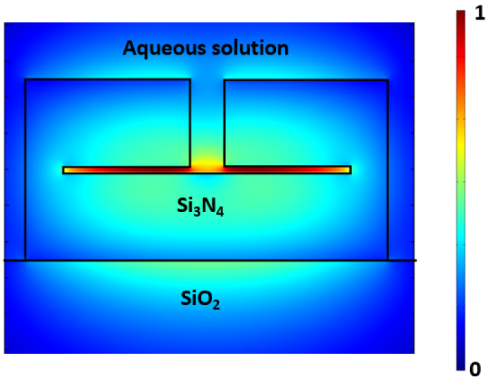

Fig. 4. Fundamental quasi-TM mode supported by the optimized waveguide. Normalized |Ey| is plotted.

We have envisaged a CMOS-compatible fabrication process of the designed device. A uniform layer of silicon nitride having thickness $h_T/2$ could be deposited on the SiO_2 substrate and then selectively etched (etch depth = $h_S/2$, width of the etched region = w_S). This step could be followed by the deposition of a uniform SiO_2 layer selectively removed from the region outside the horizontal slot. At this stage, a layer of Si_3N_4 with thickness $h_T/2$ could be deposited on the substrate and selectively etched forming the vertical slot. After that step the remaining SiO_2, acting as sacrificial material, could be removed by a selective wet etching. Finally, the device could be patterned by deeply etching the Si_3N_4 (etch depth = w_T). After manufacturing the optical chip, a sensing window for each ring resonator has to be-realized. A polymer could be deposited on the chip and then five squared sensing windows (see Fig. 1) could be opened in the polymer layer.

After the chip manufacturing, each ring has to be individually functionalized. This means that for each ring appropriate bioreceptors, capable of recognizing and specifically capturing the target biomarkers, have to be immobilized on the silicon nitride surface so forming a uniform functionalization layer. Immunoglobulin G (IgG) antibody molecules, having a Y shape (see the inset in Fig. 2) and height in the direction orthogonal to the silicon nitride surface of about 8 nm [18], have been selected as bioreceptors. Before the bioreceptors immobilization the silicon nitride surface has to be activated through an appropriate procedure depending on the bioreceptors to be immobilized. To improve the uniformity of the functionalization layer, in two sections of the ring the width of the vertical slot can be locally increased up to some hundreds of nm to create two holes in the top Si_3N_4 layer. Those holes would make easy the flow of the different solutions utilized during the activation/functionalization procedure within the reversed T shape hollow region [19,20]. We verified that the impact of those two holes on the electromagnetic propagation within the ring is negligible.

As already mentioned, the five target molecules for the fiver rings are A1AT, Cyfra 21–1, IGF1, RANTES and AFP. The target molecules have a weight ranging from 7 kDa to 70 kDa and a volume < 100 nm^3 [21–25]. For each target an appropriate IgG antibody serving as bioreceptor has to be identified and then the technique for the bioreceptor immobilization on the silicon nitride surface has to be optimized. For example, a bioreceptor with high affinity for AFP is the anti-AFP monoclonal antibody (anti-AFP). An efficient procedure for anti-AFP immobilization on the silicon nitride surface has been developed in [26].

#242374 Received 4 Jun 2015; revised 25 Sep 2015; accepted 25 Sep 2015; published 23 Oct 2015

Due to the typical size of IgG antibody molecules the thickness of the functionalization layer before the interaction with the target molecules is about 8 nm. After the interaction with the target biomarkers, the adlayer becomes irregular, with a thickness ranging from about 8 nm to about 10-12 nm (the thickness increase due to bioreceptor/biomarker binding has been evaluated according to the volume of the target molecules). The average thickness *a* of the adlayer depends on the concentration of the target biomarker in the biologic fluid interacting with the resonator.

4. Photonic chip design

The rings Q-factor strongly influences the LOD and resolution, i.e. the minimum detectable concentration of the target biomarker in the biologic fluid, usually expressed in ng/mL. Therefore, we have investigated the dependence of the Q-factor on the ring radius, by imposing an extinction ratio of 8 dB. This requirement assures that the resonance wavelength can be evaluated with high resolution (< 1 pm). The ring resonator coupled to one bus waveguide has been modelled by the transfer matrix approach [27]. We have derived a novel closed-form expression of the resonator Q-factor, without any approximation (see Appendix). We have varied the radius from 20 μm (minimum radius to avoid bending loss) to 120 μm (step = 10 μm), and for all radius values we have calculated the Q-factor. The obtained results in Fig. 5 show that, as expected, the Q-factor increases as the radius increases. A Q-factor ranging from 75,000 to 140,000 has been evaluated. We have also obtained a coupling loss of 0.5%.

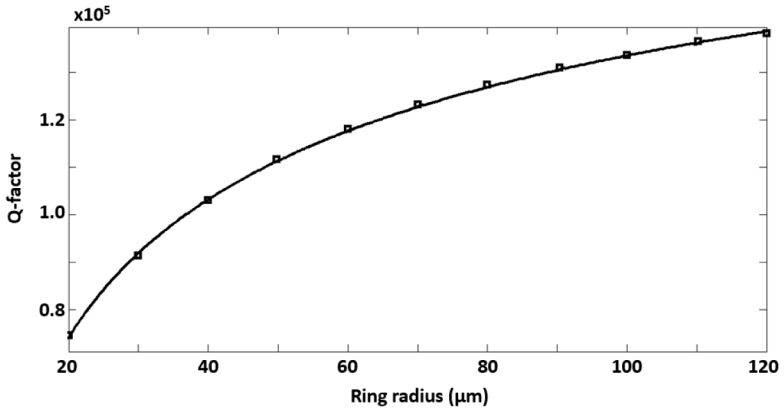

Fig. 5. Q-factor vs. ring radius. Extinction ratio of the spectral response = 8 dB.

The LOD of each ring resonator in terms of minimal detectable biomarker mass per sensing area, usually expressed in pg/mm^2, is given by [28]:

$$\mathrm{LOD} = \frac{n_{FL} - n_S}{\partial n_{FL}/\partial c} \Delta\lambda_0^{min} \left[\frac{\partial \lambda_0}{\partial a}\right]^{-1} \quad (1)$$

where n_S is the real part of the complex refractive index of the aqueous solution, c is the biomarker concentration in that solution, λ_0 is the resonance wavelength of the resonator, $\Delta\lambda_0^{min}$ is the minimum detectable shift in the resonance wavelength. For the selected biomarkers, a good approximation of $\partial n_{FL}/\partial c$ is 187 mm/g^3 [28]. As in [10], we assume that $\Delta\lambda_0^{min}$ is FWHM/200, where FWHM (= Q/λ_0) is the full-width at half-maximum of the resonator. Since the derivative of λ_0 with respect to a can be written as:

$$\frac{\partial \lambda_0}{\partial a} = \frac{\partial \lambda_0}{\partial n_{eff}} \frac{\partial n_{eff}}{\partial a} = \frac{\lambda_0}{n_{eff}} \frac{\partial n_{eff}}{\partial a}, \quad (2)$$

#242374 Received 4 Jun 2015; revised 25 Sep 2015; accepted 25 Sep 2015; published 23 Oct 2015

the LOD is equal to:

$$\mathrm{LOD} = \frac{n_{FL} - n_S}{\partial n_{FL}/\partial c} \frac{\lambda_0}{200\,Q} \left[\frac{\lambda_0}{n_{eff}} \frac{\partial n_{eff}}{\partial a} \right]^{-1}. \quad (3)$$

Equation (3) shows that the LOD depends only on the Q-factor of the ring resonator and the waveguide surface sensitivity (= 0.0011 nm^{-1}). The resolution of the ring resonator can be estimated as the ratio between the minimum mass m of analyte that can be detected by the device and the volume V of the solution directly interacting with the functionalization layer. The minimum mass can be written as m = LOD x A, being A the ring footprint. The volume V is the product between A and the thickness t_S of the fluid interacting with the sensor. From experimental data in [10], we have extracted a reasonable value of t_S = 300 μm. The dependence of the LOD and the concentration on the ring radius are shown in Fig. 6 (a) and Fig. 6 (b), respectively. Both LOD and resolution decrease and thus improve as the radius increases. The target resolution is achieved for radius > 23.5 μm. For a radius of 20 μm, as in [10], the archived LOD is about 0.06 pg/mm^2, five times better than the state-of-the-art (0.3 pg/mm^2) [10]. For a radius of 20 μm, we have investigated the degradation of the LOD due to an increase δ, due to fabrication tolerances, of the most critical dimension of the design, i.e. h_S (see Fig. 7). As expected, the percentage degradation of the LOD increases as δ increases. We have verified that the degradation of the LOD is < 8% if δ is ≤ 10 nm.

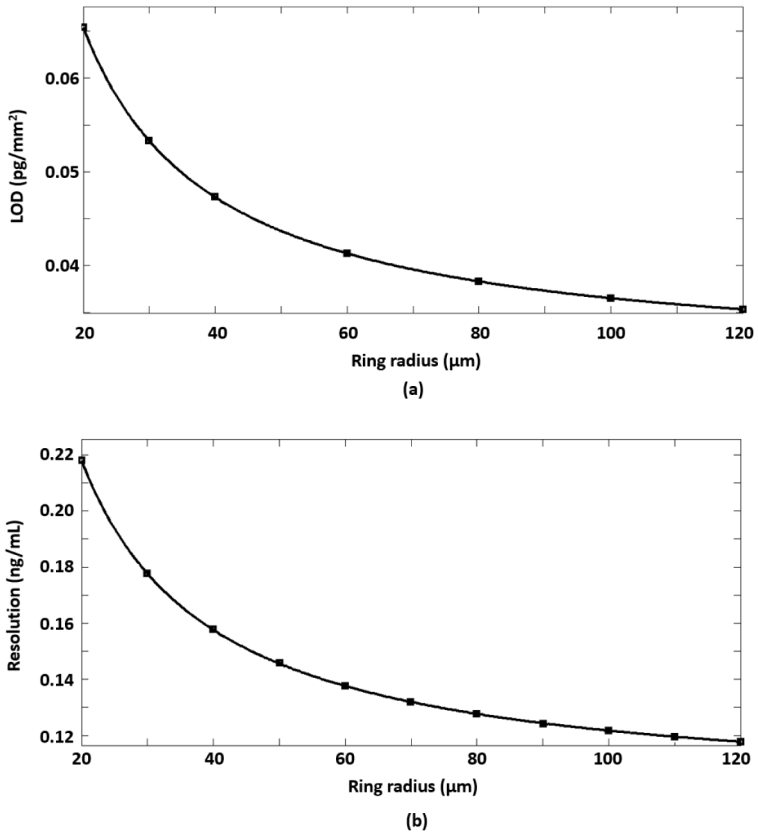

Fig. 6. (a) LOD dependence on the ring radius. (b) Resolution as function of the radius.

#242374 Received 4 Jun 2015; revised 25 Sep 2015; accepted 25 Sep 2015; published 23 Oct 2015

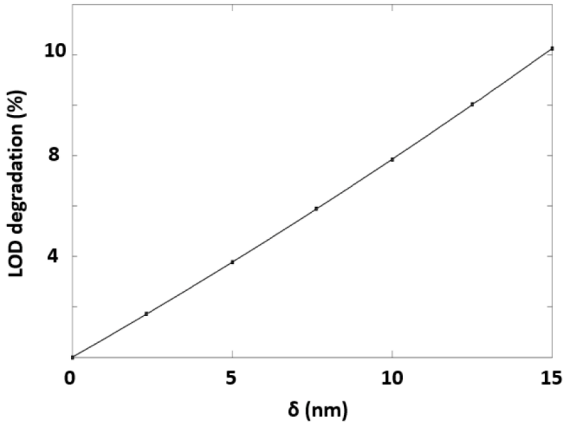

Fig. 7. (a) LOD degradation vs. δ, for a ring radius = 20 μm.

Due to the selected sensor configuration, the radii of the five rings have to be all different. We selected the radii assuming the distance between two adjacent resonance frequencies of about 1 nm, which is about 50 times larger than the FWHM. The radii of the rings are R_1 = 23.538 μm, R_2 = 23.556 μm, R_3 = 23.574 μm, R_4 = 23.592 μm, and R_5 = 23.611 μm. The distance between the centers of two adjacent rings is assumed equal to 150 μm. Thus the sensor footprint is about 750 μm x 50 μm = 37,500 μm^2 = 0.0375 mm^2. The normalized optical spectrum at the sensor output when no biomarker is in the biologic fluid interacting with rings is shown in Fig. 8. The spectrum shows five resonances, each relevant to a ring, in the spectral range from 1299 nm to 1305 nm. By tracking the five resonances, the sensors estimates the concentration of the five target biomarker in the biologic fluid.

By using experimental data in [10], we assumed that the immobilization technique allows a density of binding site (bioreceptors that can bind to the target biomarkers) of 10^{10} per mm^2. This means that the number of binding sites for each ring resonator is 10^{10} x A = 2.2x10^7. The maximum mass of target analyte that can be sensed by each ring is the product between the molecular mass of the target molecule and the number of binding sites for each resonator. If the molecular mass of the target molecule is about 50 kDa (= 8.3x10^{-20} g), as for the A1AT, the maximum mass that can be sensed is 1.66x10^{-12} g. The ratio, equal to 2500 ng/ml, between that mass and V is the maximum concentration of target molecule that can be sensed by each ring. This means that the sensor dynamic range is approximately 40 dB. This value of dynamic range is complaint with the application of the biosensor.

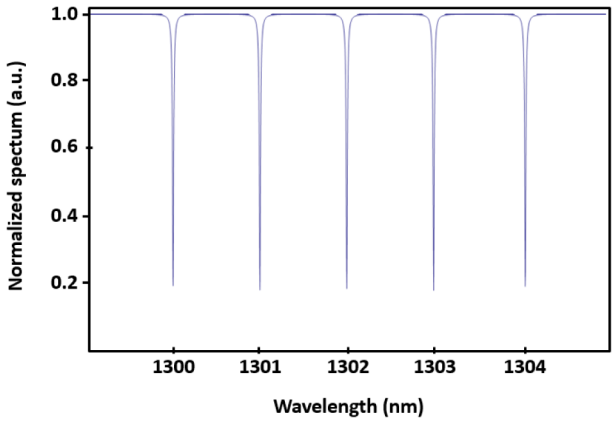

Fig. 8. Normalized optical spectrum at the output of the bus waveguide when the concentration of all biomarkers in the biologic fluid under analysis is zero.

#242374 Received 4 Jun 2015; revised 25 Sep 2015; accepted 25 Sep 2015; published 23 Oct 2015

The coupling efficiency η between the bus waveguide and each ring has to be 0.4% for all rings. This value allows the achievement of the requirement on the extinction ratio (= 8 dB). The couplers included in the device are formed by a straight waveguide and a bent one (see Fig. 9). In this component, the distance d between the centers of the waveguides depends on z, i.e. the coordinate along the propagation direction, and so the coupling coefficient κ between the modes propagating in the two waveguides depends on z, too.

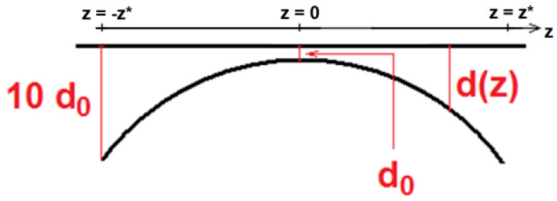

Fig. 9. Coupler formed by a straight waveguide and a bent one.

The distance between the waveguides is equal to:

$$d(z) = R + d_0 - \sqrt{R^2 - z^2} \tag{4}$$

where R is bending radius of the bent waveguide and d_0 is the minimum distance between the centers of the waveguides.

The dependence of the coupling coefficient κ on d has been derived by calculating the propagation constants of the symmetric and the anti-symmetric quasi-TM supermodes (β_S and β_A, respectively) supported by the coupler for d ranging from 1100 nm to 1800 nm. The coupling coefficient κ is equal to $(\beta_S - \beta_A)/2$ [29]. The κ dependence on d is very well fitted by the following exponential function:

$$\kappa(z) = K_1 \exp\left[K_2\, d(z)\right] = K_1 \exp\left[K_2 \left(R + d_0 - \sqrt{R^2 - z^2}\right)\right] \tag{5}$$

where K_1 (= 1.751 x 10^7 m^{-1}) and K_2 (= –4.502 x 10^6 m^{-1}) are fitting coefficients depending on the geometrical and optical properties of the waveguides forming the coupler.

The amplitudes A_1 and A_2 of the two modes propagating in the waveguides can be estimated by using the coupled mode theory (CMT) [30]:

$$\begin{cases} \dfrac{dA_1(z)}{dz} = -i\,\kappa(z)\,A_2(z) \\ \dfrac{dA_2(z)}{dz} = -i\,\kappa(z)\,A_1(z) \end{cases}. \tag{6}$$

For $z = \pm 3\sqrt{2\,d_0^2\,R - 9\,d_0^2} = \pm z^*$ the distance between the waveguides is $10d_0$. We can assume that the coupling between the waveguides is negligible at that distance. Therefore we simulate the coupler in the range from -z* to + z* and impose the following initial condition:

$$a_1(-z^*) = 1 \quad , \quad a_2(-z^*) = 0. \tag{7}$$

The coupling efficiency η, which is the fraction of the optical power passing from the straight waveguide to the bent one, can be estimated by solving the equation system (6) in the range from -z* to + z*.

After calculating the solution of Eq. (6), the coupling efficiency can be evaluated as:

$$\eta = \left|a_2(z^*)\right|^2 . \tag{8}$$

#242374 Received 4 Jun 2015; revised 25 Sep 2015; accepted 25 Sep 2015; published 23 Oct 2015

The coupling efficiency vs. the gap between the bus waveguide and the ring is shown in Fig. 10. As expected η decreases as the gap increases. The condition η = 0.4% is achieved for gap = 636 nm.

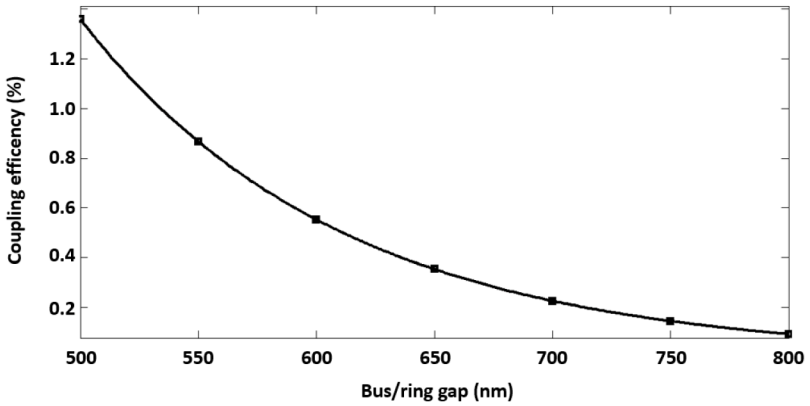

Fig. 10. Coupling efficiency vs. the gap between the straight bus waveguide and the ring.

Finally, we have theoretically evaluated the thermal sensitivity of the ring resonators. As in [31], the thermo-optic coefficients of the aqueous solution, the silicon nitride and the silicon oxide have been assumed equal to -10^{-4} RIU/K, 10^{-5} RIU/K, and 10^{-5} RIU/K, respectively. We have obtained a thermal sensitivity of 15 pm/K. This result is slightly better than that one obtained in [31] for silicon nitride slotted ring resonators having a radius of 70 μm.

5. Conclusions

A CMOS-compatible integrated optical biosensor with footprint = 0.0375 mm^2 for the simultaneous detection of five selected lung cancer biomarkes with resolution 0.2 ng/mL has been designed, envisaging also the device fabrication process. The sensor includes five Si_3N_4/SiO_2 ring resonators with a novel configuration evanescently coupled to one straight bus waveguide. Each micro-cavity has a LOD depending on the ring radius and ranging from about 0.06 pg/mm^2 to about 0.03 pg/mm^2 as the radius varies from 20 μm to 120 μm. Since the state-of-the-art achieved by a ring resonator with radius 20 μm is 0.3 pg/mm^2, the new ring resonator configuration improves it of five times. The reported new way for improving the LOD of ring resonator biosensors is extremely general and can be useful for the detection of a wide range of target molecules that are of interest for several application domains, e.g. some areas of medicine, environmental monitoring, and homeland security.

Appendix

The spectral response of a resonator coupled to one bus waveguide is given by [27]:

$$T(\nu)=\frac{\sqrt{\gamma-\eta}-\gamma\, e^{i\beta L}\, e^{-\alpha L/2}}{1-\sqrt{\gamma-\eta}\, e^{i\beta L}\, e^{-\alpha L/2}}=\frac{\gamma+\gamma^2 e^{-\alpha L}-\eta-2e^{-\alpha L/2}\gamma\sqrt{\gamma-\eta}\cos(\beta L)}{1+e^{-\alpha L}(\gamma-\eta)-2e^{-\alpha L/2}\gamma\sqrt{\gamma-\eta}\cos(\beta L)} \tag{9}$$

where $\beta=(2\pi\nu n_{eff})/c_0$, ν is the frequency, and c_0 is the speed of light in vacuum.

The maximum and the minimum of T(ν) are equal to:

$$T_{max}=\frac{\gamma+\gamma^2 e^{-\alpha L}-\eta+2\gamma\sqrt{\gamma-\eta}\, e^{-\alpha L/2}}{1-(\gamma-\eta)e^{-\alpha L}+2\gamma\sqrt{\gamma-\eta}\, e^{-\alpha L/2}}, \tag{10}$$

#242374 Received 4 Jun 2015; revised 25 Sep 2015; accepted 25 Sep 2015; published 23 Oct 2015

$$T_{min} = \frac{\gamma + \gamma^2 e^{-\alpha L} - \eta - 2\gamma\sqrt{\gamma-\eta}\, e^{-\alpha L/2}}{1-(\gamma-\eta)e^{-\alpha L} - 2\gamma\sqrt{\gamma-\eta}\, e^{-\alpha L/2}}. \quad (11)$$

By solving the following equation:

$$T(\nu) = T_{min} + \frac{T_{max} - T_{min}}{2} \quad (12)$$

we obtain two solutions denoted as ν_1 and ν_2 (Fig. 11).

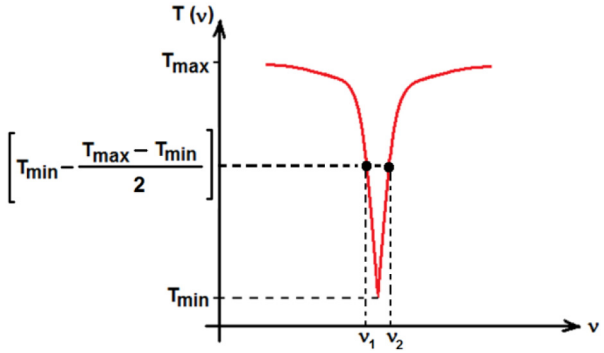

Fig. 11. Spectral response of the ring resonator coupled to one bus waveguide.

The quality factor of the ring resonator is equal to:

$$Q = \frac{\nu_0}{\nu_2 - \nu_1} = c\left[4\pi\nu_0 \left| \frac{Ln_{eff}\, \arccos\left(\frac{2e^{\alpha L/2}\sqrt{\gamma-\eta}}{\gamma-\eta+e^{\alpha L}}\right)}{\left(\operatorname{arcosh}\left(\frac{2e^{\alpha L/2}\sqrt{\gamma-\eta}}{\gamma-\eta+e^{\alpha L}}\right)\right)^2 + \frac{4\pi^2 L^2 n_{eff}^2 \nu_0^2}{c^2}} \right| \right]^{-1} \quad (13)$$

This is an original expression of the Q-factor of a ring resonator coupled to a bus waveguide, that we have derived without any physical or numerical approximation.

#242374 Received 4 Jun 2015; revised 25 Sep 2015; accepted 25 Sep 2015; published 23 Oct 2015